Hewlett Packard Labs

Multiple Chip Module Cooling Using Vapor Chamber

Sergio Escobar-Vargas, Niru Kumari, Ernesto Ferrer, Rocky Shih, Sarah Anthony, Joshua Hrisko, Zhimin Wan

Hewlett Packard Labs
HPE-2016-85

Keyword(s):
Vapor chamber; power map; thermal resistance; dynamic response

Abstract:
This document describes the characterization of vapor chambers as cooling devices for multiple chip modules. The work consists of experiments and theory of vapor chambers. It includes developing and building the testing system, selecting the control and monitoring parameters, designing the vapor chamber, performing experiments, analyzing measurements, and drawing recommendations for vapor chamber selection and operation. The experiments include typical operation conditions found in electronics e.g. power dissipations up to 250 W, power densities up to 100 W/cm^2, and operating temperatures up to 45 C among other parameters. The main outcome of this work is that vapor chamber performs better than a solid heat spreader under specific conditions and the guidelines are included in the conclusions section; other outcomes include correlations and quantification of vapor chamber thermal resistance functionality to the control parameters.

External Posting Date: October 19, 2016 [Fulltext]
Internal Posting Date: October 19, 2016 [Fulltext]

Hewlett Packard Enterprise

Multiple Chip Module Cooling Using Vapor Chamber

Sergio Escobar, Niru Kumari, Ernesto Ferrer, Rocky Shih,

Sarah Anthony, Josh Hrisko, & Zhimin Wan

Contents

1 Abstract

This document describes the characterization of vapor chambers as cooling devices for multiple chip modules. The work consists of experiments and theory of vapor chambers. It includes developing and building the testing system, selecting the control and monitoring parameters, designing the vapor chamber, performing experiments, analyzing measurements, and drawing recommendations for vapor chamber selection and operation. The experiments include typical operation conditions found in electronics e.g. power dissipations up to 250 W, power densities up to 100 W/cm^2, and operating temperatures up to 45 C among other parameters. The main outcome of this work is that vapor chamber performs better than a solid heat spreader under specific conditions and the guidelines are included in the conclusions section; other outcomes include correlations and quantification of vapor chamber thermal resistance functionality to the control parameters.

2 Introduction

The integrated circuits miniaturization, the integration of several components under the same package, and the space reduction in systems (e.g. servers, PCU, and phones) is pushing the limits of air cooling methods; at some instances air cooling is unable to solve the problems of high temperatures, surfaces with non-uniform temperatures, and dynamic temperature profiles. Therefore, to address these problems different cooling methods and components are used e.g. heat pipes, cold plates, as well as liquid cooling on its different forms. The resistance to adopt liquid cooling is strong in the IT industry; it is automatic to first look at potential air cooled systems, no matter how complicated they may be, before turning into liquid cooling.

An attractive solution to multiple chip module cooling is the use of vapor chambers (VC). VCs take advantage of the change of phase of a liquid to provide enough cooling to the IC and still enable the use of air cooling at the heat sink. VC performance is difficult to establish considering the complex physics occurring inside the VC. An example of traditional VC analysis follows.

The most traditional form of quickly simulating a VC is assuming constant thermal conductivity (order of 10^3 W/m-K). Figure 1 shows the simulation results of cooling a multiple chip component (Intel KNL) cooled with: a solid heat sink with aluminum (Al) base and Al fins; a solid heat sink with copper (Cu) base and Al fins; and an Al VC as the base for Al fins. Air flows at 20 CFM with no bypass and the multiple chip generates a total of 221 W (one CPU at 205W and sixteen memory blocks at 16W).

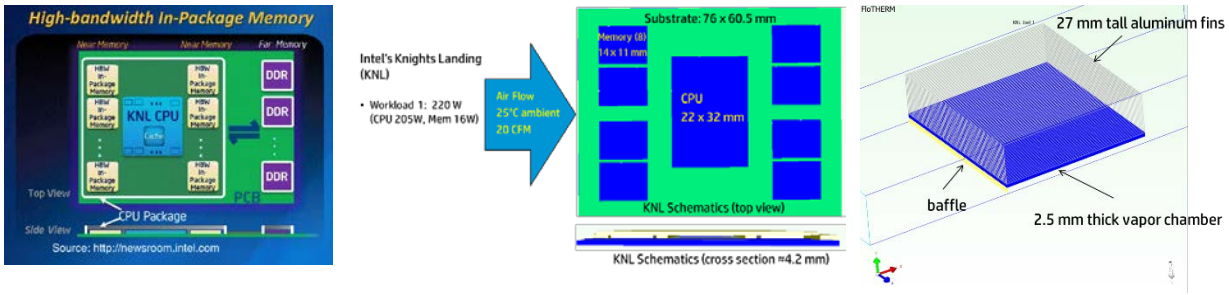

a b c

Figure 1. Model to simulate the cooling of a package with multiple internal components. a) illustration of the Knight Landings (KNL) package from Intel; b) KNL schematic for the model; c) Flotherm model with the heat sink attached to the package

The heat sink design is 113 x 100 x 27 mm (W x L x H); aluminum fins; uniform fins; 88 fins; 0.3 mm thick fin. The temperature profiles provide information on the temperature distribution and the magnitude of the maximum temperature reached for each one of the considered cases (Figure 2). The thermal conductivities from Al and Cu are in the Flotherm library, the thermal conductivity for the VC is 5000 W/m-K which is a typical value used to represent VCs. The model is solved as a thermal conduction problem.

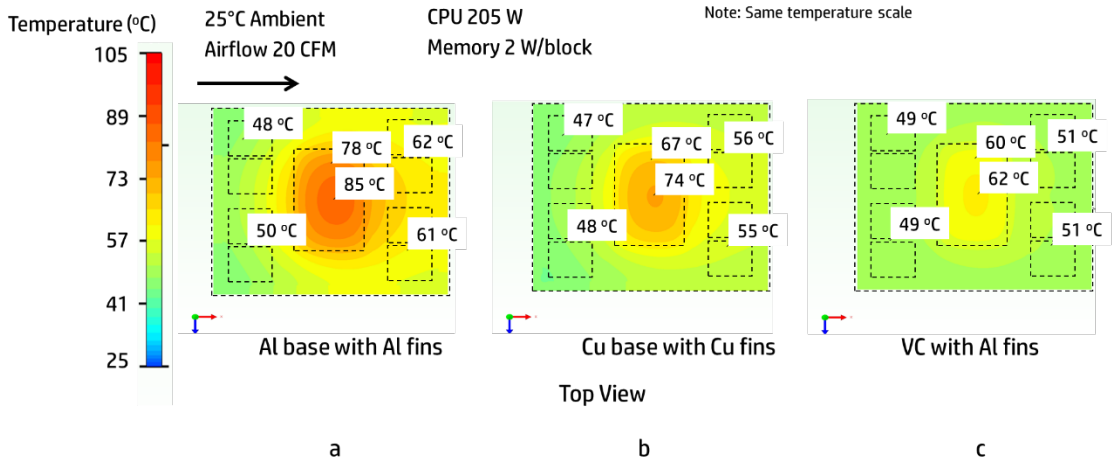

a b c

Figure 2. Temperature distribution at the KNL package lid. Assuming a VC with constant (k=5000 W/mK)

The maximum temperature occurs when the package is cooled with the aluminum base and fins due to the lower conductivity of this material; the maximum temperature is where the component with the maximum heat generation occurs, in this case the CPU at the center. The temperature differences on the case decrease when higher thermal conductivity materials are used (see Figure 2c). The non-uniform temperature at the base of the heat sink causes some fins to operate at temperatures slightly warmer than ambient temperature (Figure 3); this results in poor heat dissipation through the heat sink. It is therefore important to provide a uniform base temperature at the heat sink to better use the fins

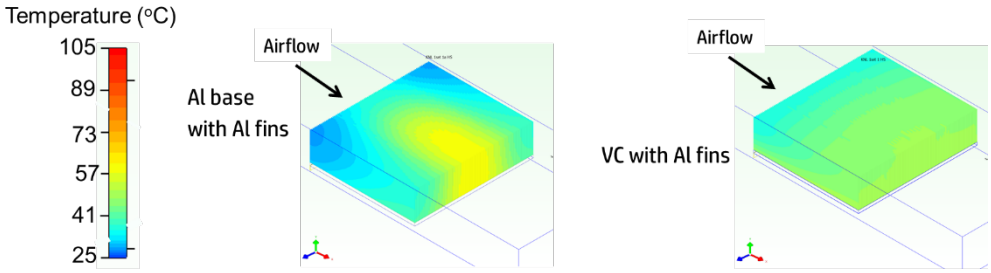

Figure 3. Temperature distribution on the fins of a heat sink attached to an element with a hot spot at the center. a) Aluminum solid heat sink, base and fins; b) Aluminum vapor chamber at the base with aluminum fins

3 Experimental setup

3.1 Description

The testing bench (Figure 4) is an upgraded version of a bench for liquid cooling testing of cold plates [Escobar, 2014], it has a temperature controller (ThermoRack 800, Solid State Cooling Systems) with integrated pump and fluid reservoir. The cooling liquid is a mixture of water and glycol (LIQ-702, Koolance). The bench has a flow meter (+GF+SIGNET 2000-11 Micro Flow Sensor), differential pressure (PX81D0-020DI, Omega), and thermocouples attached (T type, Omega). A cold plate (CP) is attached to the coolant fluid loop by means of insulated piping (44745K21, McMaster-Carr); the cold plate bottom surface is in contact with the vapor chamber (VC) top side, on the other side of the VC is the thermal test vehicle (TTV). The cooling fluid temperature is set at the temperature controller, the integrated pump delivers a constant flow rate; the flow rate through the CP is controlled through the means of valves in the fluid loop. The flow passes through the measuring flow rate device, it enters and exits the cold plate to return to the temperature controller and close the loop. A couple of thermocouples measure the temperature at the input and output of the cold plate. The temperature difference in the fluid is due to the energy absorbed by the CP from the VC.

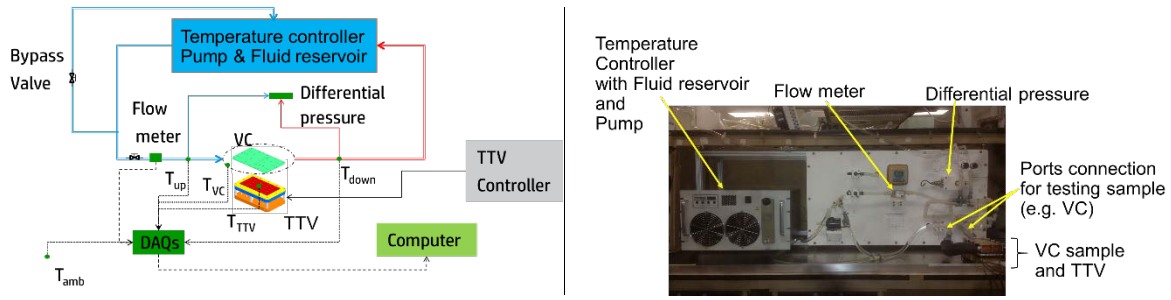

a b

Figure 4. Experimental set up: a) Schematic description of the test bench; b) Actual wet bench

A couple of data acquisition units (Agilent 34970A) records the temperatures from all the sensors and then save the data as csv files.

3.2 Thermal Test Vehicle (TTV)

The TTV has an array of five by five electric heaters embedded in copper blocks, this is a custom built TTV. The fixture material is Al for structural rigidity and Ultem for thermal insulation. The Cu blocks have a hot surface in contact with the VC. Two different hot surface sizes are used, the small size (5 mm x 5 mm) helps to achieve high heat fluxes with relatively low power, the large size (12 mmx 24 mm) helps to reach the maximum VC power dissipation without incurring in temperatures larger than 100 ^{o}C.

The TTV fixture has fixed size slots for blocks of 12 mm x 24 mm, thus the small heater is complemented with an insulation envelope to fit it in the slots (Figure 5b).

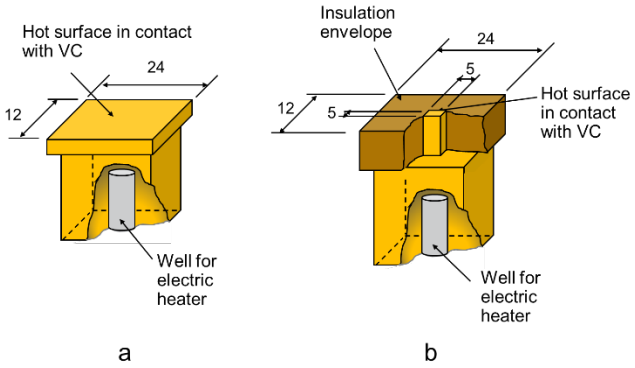

Figure 5. Copper blocks with well for electric heater and exposed hot surface area of size: a) 12 mm x 24 mm; b) 5 mm x 5 mm and with Ultem insulation envelope

The Cu block heaters have a well to insert an electrical heater. The electric heater is inserted using thermal grease to improve the thermal contact between the heater and the copper block. The cylindrical electric heater is custom made (HSK1812699, OMEGA) with physical dimensions of 25.4 mm long and 6.35 mm diameter and capable to deliver up to 200 W.

The electric heaters and Cu blocks sit in a fixture made out of Aluminum and Ultem (Figure 6a). The bottom part of the fixture is open to ambient; a compression resistant polymide insulation (93015K62, McMaster-Carr) in between the copper blocks, not shown in the figure, reduces the heat losses from the bottom of the TTV. The VC sits on top of the TTV Cu blocks and the CP sits on top of the VC (Figure 6b), thermal interface material (X23-7762-S, Shin+EtsuMicroSi) in between increases the thermal conductivity at the interfaces in contact.

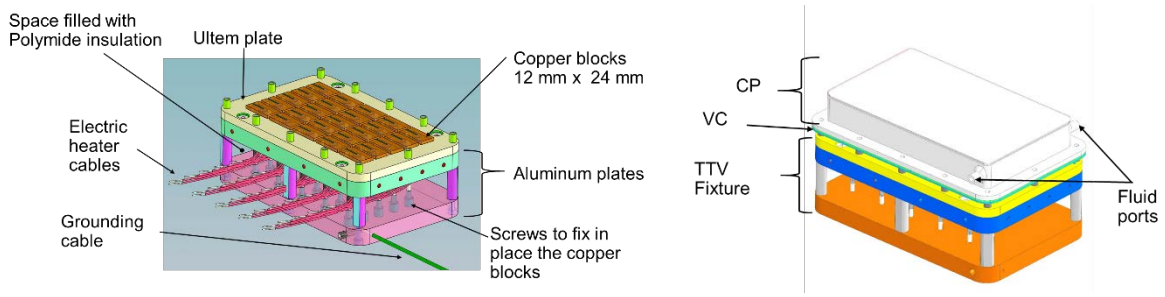

a b

Figure 6. Thermal test vehicle: a) TTV fixture with copper blocks and electric heaters; b) Schematic of TTV-VC-CP assembly

Custom built hardware and software control the electric heaters. This controller unit is capable of delivering up to 30 Amps and 120 V, therefore the fixture must be physically grounded for safety reasons. Figure 7 shows the interfaces to control the active heater/s and time duration. Each one of the boxes represents a heater block and its relative location within the five by five array. The controller allows the activation of any heater by typing manually (Figure 7a) on the heater to be activated; the field accepts integer numbers from 0 to 100, the number entered is a percentage of the electric heater power. The controller also allows programmable activation (Figure 7b). The user should generate a csv file indicating what heaters activate and how many cycles they should stay active. When operating in programmable mode, the controller interface displays the heaters and power percentage of activation as well as a regressive counter indicating how many cycles remain to end the batch. The cycle counter unit display the remaining cycles as well as a factor of 0.833 secs, multiplying the remaining cycles by the factor provides the actual remaining time in secs. Red squares with no numbers on the programmable interface indicate those heaters were not set thus they are not active.

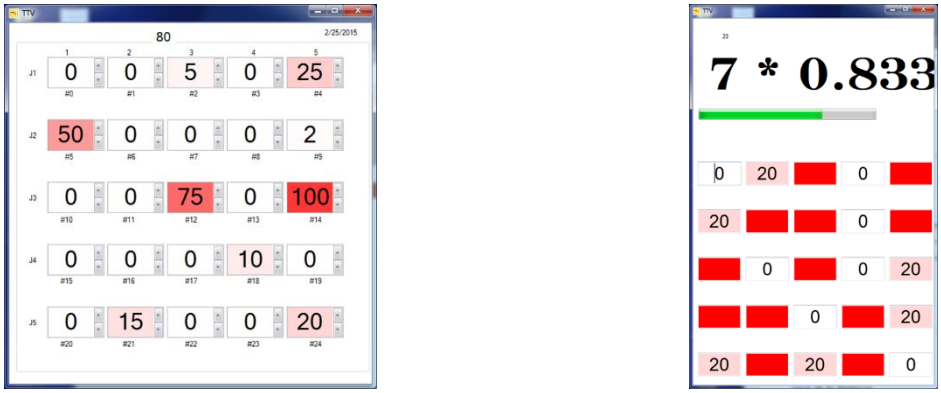

a b

Figure 7. Heater controller interfaces: a) Manual; b) Programmable

Two data acquisition (DAQ) units collect the data from the temperature sensor at the TTV, wet bench, and VC; the cooling fluid flow rate is measured as well. Figure 8 is a snippet of the interface after

setting up the two DAQs to read more than sixty thermocouples and a flow meter. The data is stored in a computer and later analyzed with Matlab and Excel.

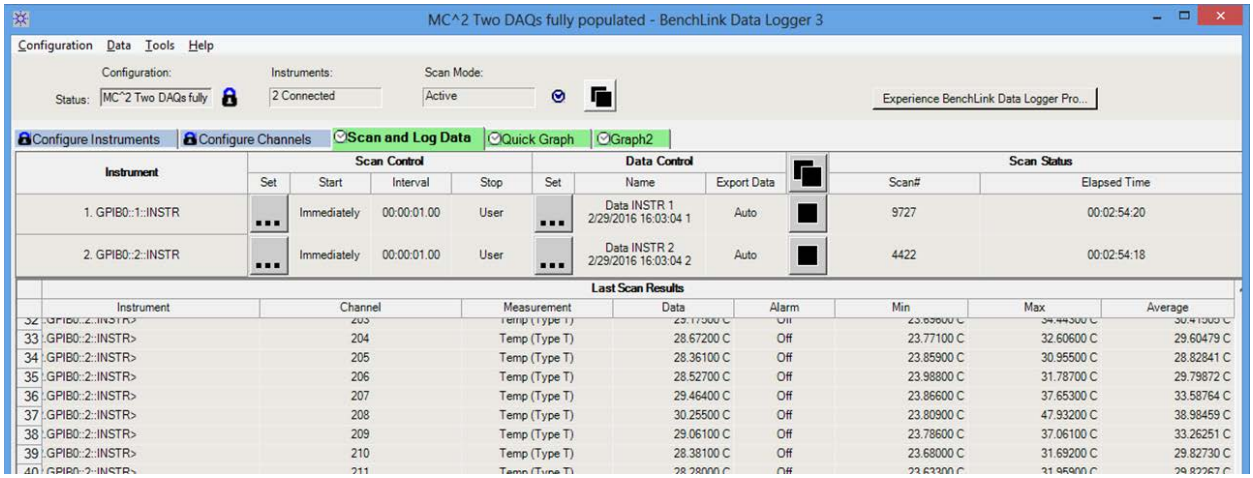

Figure 8. Data acquisition Interface to set the sensors

3.3 Vapor Chamber (VC)

Two cold plates and three vapor chambers are custom built (by Thermacore). The VCs have a layer of uniform wick in the bottom plate and no wick at the top plate. Figure 9 is a schematic side view of a cut to show the VC dimensions and internal structure, the vapor core is a continuous layer with pillars at some locations, the pillars provide structural rigidity. The thickness of the evaporator, wick, and condenser layer is the same for the three tested VCs. The wick layer sits on top of the evaporator layer and around the pillars; the wick has uniform thickness. The VC total area is 144 mm x 84 mm

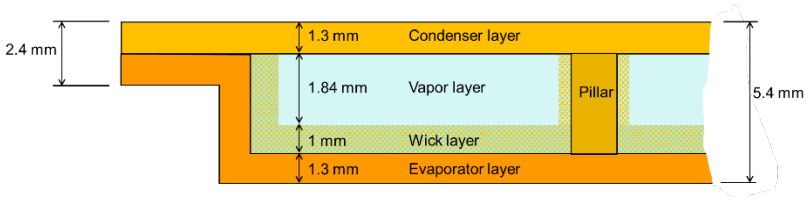

Figure 9. Vapor chamber internal layers. Example for vapor core thickness of 1.84 mm; the second VC has a thickness of 0.75 mm. Not to scale

Three VCs are tested to investigate the effect of vapor core thickness and wick capillarity. Table 1 shows the features for each of the VCs

Table 1. Vapor chambers parameter values.

Label	Parameters	Value
VC1	Vapor core thickness	1.84 mm
	Wick powder	Red
VC2	Vapor core thickness	0.75 mm
	Wick powder	Red
VC3	Vapor core thickness	1.84 mm
	Wick powder	Black

Changing the wick powder changes the capillarity, this will provide insight on the VC capillary limit; the manufacturer did not disclose the capillary value for the two kind of powders thus they will be referred as “Red” and “Black”. Changing the vapor core thickness would provide insight on the sonic limit, this is a limit that could be reached if the VC is too thin; the interest in thin VC is because extremely thin VCs are in demand in electronic cooling due to space limitations in the systems. The porosity is estimated for open vapor chamber plates having red powder; the methods of image analysis and weight result in porosity of 0.5. No open chamber with black powder is available thus no porosity information is available for the black powder.

Thirty eight thermocouples measure the VC temperature on the VC external surfaces of which twenty five on the evaporator side and thirteen on the condenser side. The thermocouples are placed in grooves machined on the VC. Figure 10a is a schematic of the VC grooves on the condenser side and Figure 10b shows the internal structure of the VC to illustrate the pillars described in Figure 9.

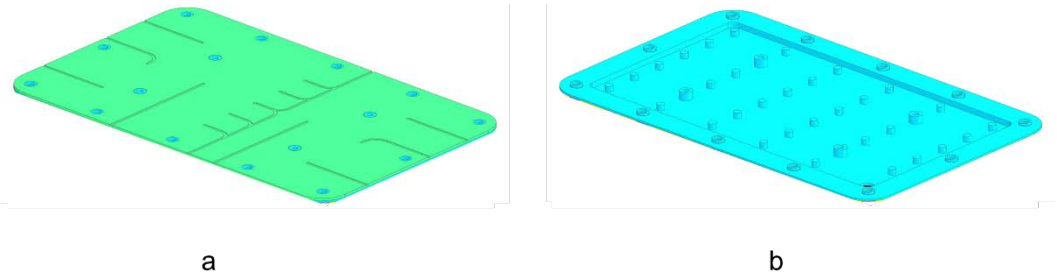

Figure 10. Vapor chamber schematics: a) Vapor chamber with machined thermocouple grooves on the condenser side; b) Pillars distribution inside a vapor chamber

Figure 11b shows the thermocouple mapping relative to the array of twenty five locations for: the TTV, VC evaporator side, and VC condenser side. The thermocouples at the copper blocks are centered on the hot surface, the thermocouples at the VC evaporator side match the location of the ones on the TTV, and the thermocouples at the VC condenser side are symmetric and match the location of some

sensors at the evaporator side. Figure 11a depicts a side view of the system TTV-VC-CP; the thermocouples locations in the TTV, VC, and CP; and the thermal interface material (TIM).

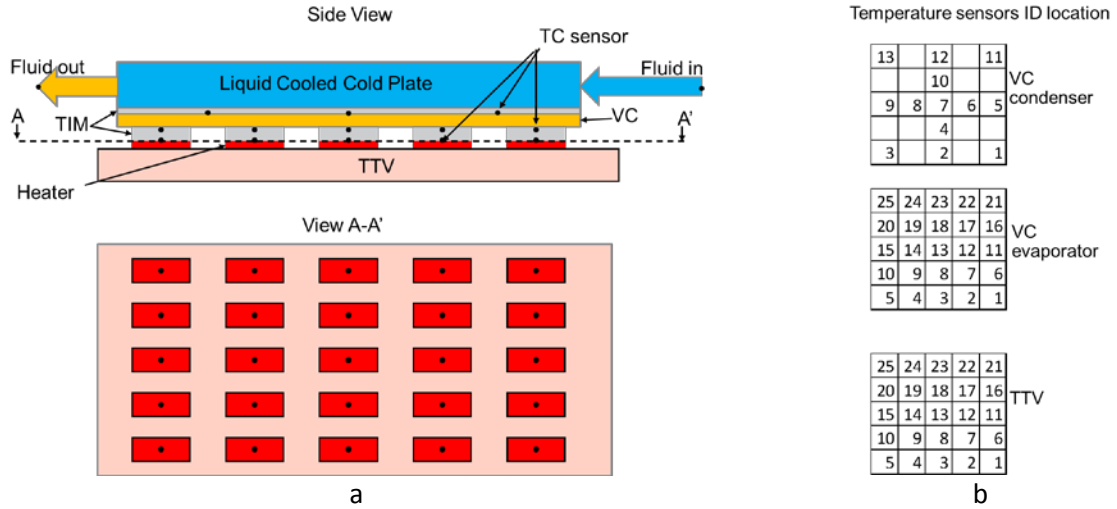

Figure 11. Thermocouples layout: a) Schematic side view for the fixture of TTV-VC-CP and section cut to show the copper blocks five by five array and thermocouple location; b) Labeling for the thermocouples location

4 Experiments

4.1 Description

Table 2 lists the parameters changed during experiments and the intent behind each experiment. It is of interest to investigate the VC limits of: capillarity, boiling, and sonic; the VC performance response when multiple heat sources is of interests as well as the dynamic response.

Table 2. Experimental parameters changed during experiments.

Parameter	Min	Max	Units	Details	Investigation Goal
Capillarity (VC powder)	Black	Red	NA	Varies permeability	Capillary limit
VC vapor core thickness	0.75	1.84	mm	Restricts the vapor transport	Sonic limit
Power	3	300	W	Total power with 1-25 heaters	Boiling limit; $R_{VC} = f(P)$
Power density	1	100	W/cm^2	Boiling, heating rate	Boiling limit; $R_{VC} = f(P/A_h)$
CP input temperature	25	45	°C	Changes operating temperature	Viscous limit
Heater location	Center	Corner	NA	Effect of spreading	$R_{VC} = f(x, y)$
Heater size	5x5	12x24	(mm)^2	Effect of spreading	Spreading resistance

The vapor chamber (Red powder, 5.44mm) time constant τ is calculated using Eq. 1 [Bergman et al, 2011] and the measured temperature decay from different heaters (18, 13, 8, 3) on the VC evaporator side resulting in an average 41.3s this number has a maximum statistical uncertainty fraction of 0.20. The statistical uncertainty is calculated using the Student's t-test method [Holman,1994].

$$\frac{T - T_{amb}}{T_i - T_{amb}} = e^{-\left(\frac{t}{\tau}\right)} \quad \text{Eq. 1}$$

The experiments uncertainty is calculated for the thermal resistance and using the Student t-test statistical method. The maximum uncertainty is 0.20, a median of 0.07, a small set of tests exceeded 0.20 and these experiments are not considered in the results.

4.2 Results

The thermal resistance "*R*" is the metric used to report the experimental results, the thermal resistance being defined as

$$R = \frac{T_{max_{evaporator}} - T_{avg_{condenser}}}{\dot{Q}_{CP}} \quad \text{Eq. 2}$$

Where $T_{maxevaporator}$ is the maximum temperature at the VC evaporator side [C], $T_{avgcondenser}$ is the average temperature of all the thermocouples at the VC condenser side [C], $\dot{Q}_{CP}$ is the power (heat flow rate) captured by the fluid passing through the cold plate and it is calculated using

$$\dot{Q}_{CP} = \dot{m} c_p (T_{out} - T_{in}) \quad \text{Eq. 3}$$

Where $\dot{m}$ is the liquid flow rate through the cold plate [kg/s], c_p is the liquid specific heat [J/(kg*C)], T_{out} is the liquid temperature at the exit of the cold plate [C], and T_{in} is the liquid temperature at the entrance of the cold plate [C].

Figure 12 indicates the VC thermal resistance decreases when the power is increased until it converges to a minimum value; this is an advantage for VCs over solid heat spreaders (SHSs), SHSs have constant thermal resistance. The data in Figure 12 is separated in series indicating the location of the heat source as well as the number of active heat sources; these cases are illustrated in the schematics at the top of Figure 12. The numbers indicate the percentage form of the ratio $\frac{A_{heaters}}{A_{VC}}$ where $A_{heaters}$ is the total area covered by the active heaters, A_{VC} is the vapor chamber area.

The current practice to select a vapor chamber is by considering the power to be dissipated and the desired thermal resistance. However looking at Figure 12 we can say the combination of power vs thermal resistance is not enough to properly select a VC, it is clear from Figure 12 that when we reach small thermal resistances with high powers, the performance is limited to very low power densities (as shown in Figure 12b); it is clear the thermal resistance follows a similar trend with power density, low

thermal resistance for high power densities. Therefore *the VC selection should be done considering the desired power density as well*. From now on, the same data is presented in the form of "P vs R" and "P/A vs R"

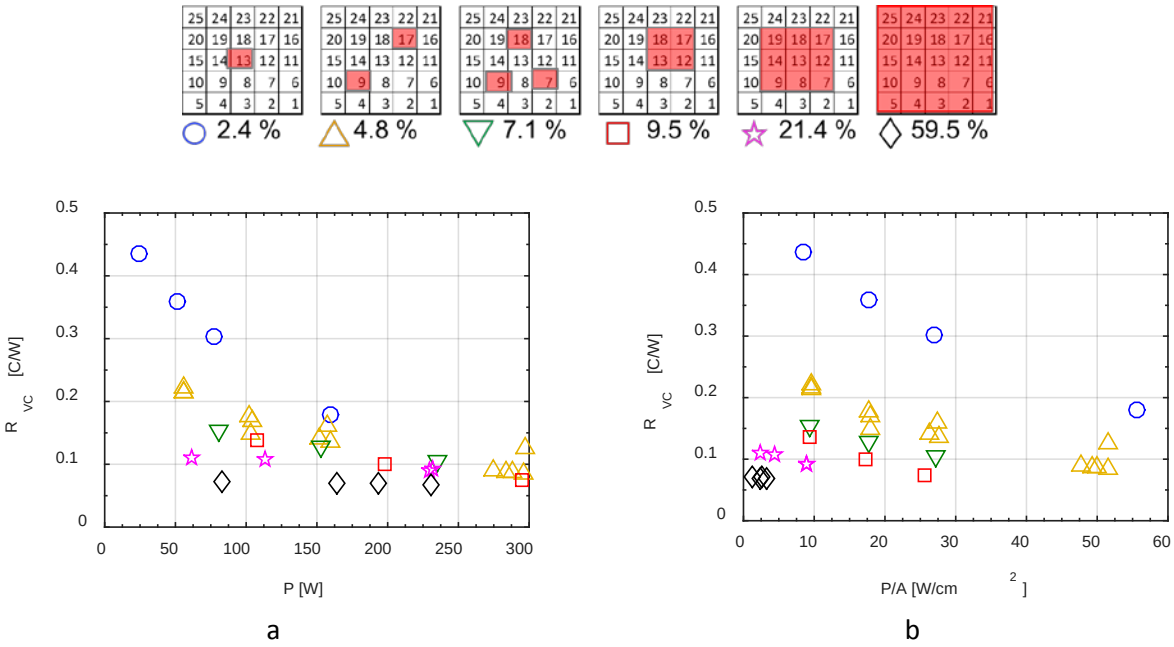

Figure 12. Thermal resistance variation with: a) Power and active heater fraction area; b) Thermal resistance variation with power density and active heater fraction area. VC is 5.4 mm thick and it has red powder

Figure 13 shows the normalized thermal resistance for three different locations for the same cooling device, either a VC or a SHS. The normalization is done respect to the location at the center in the same device e.g. $\frac{R_{SHS}}{R_{SHS_{Center}}}$ for the SHS, or $\frac{R_{VC}}{R_{VC_{Center}}}$ for the VC. The thermal resistance locations are: center, at the side in the middle, and at the corner. The normalization ratio R/R_{Center} is always 1. Values for the ratio $R/R_{Center}>1$ indicate the thermal resistance increases respect to the center; $R/R_{Center}<1$ indicates thermal resistance decreased respect to the center.

For purposes of comparison two data series are plotted, one is the VC and the other is data for the SHS. Figure 13 shows the SHS offers its best thermal resistance when the heat source is centered; on the other hand, the VC presents a thermal resistance independent of the heat source location. The variations on thermal resistance for VC at the "Half side" fall within the thermal resistance uncertainties. *The VC thermal resistance independence of heat source location is an important outcome when space constrains for cooling devices are required*.

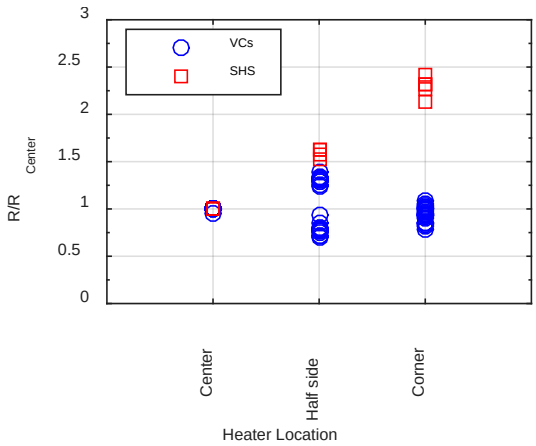

Figure 13. Effect of location for a single active heater, normalized by the resistance at the center for each test

Several experiments are performed at different operating temperatures within the range of 23-67 ^{o}C and *no correlation between the VCs performance and the operating temperatures*. The operating temperature is defined as the average temperature from all the sensors attached to the VC. Similarly the effect of the initial operating temperature shows *no correlation with the VC performance for the range of the current experiments*.

A metric used to compare the VC performance to a solid heat spreader and calculating the ratio R_{VC}/R_{SHS}. Values of $R_{VC}/R_{SHS} < 1$ indicate the vapor chamber performs better than the solid heat spreader. Figure 14 shows the results for the ratio when using a VC with: black powder, 1.875 mm vapor core, and 5 mm x 5 mm coper heaters. The results include cases for different heater locations as well as the percentage area fraction depicted on top of Figure 14. *The VC outperforms the SHS when the active heat source is off the center, the farthest off the center the better the VC outperforms the SHS. The better performance is still present when more than one heat source is active.*

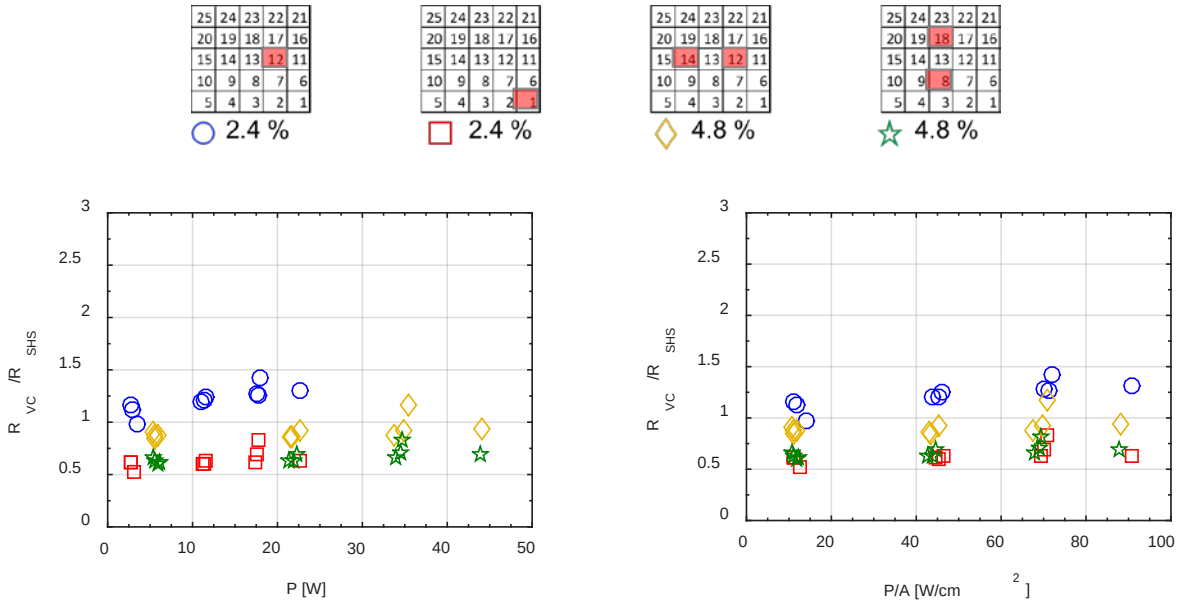

Figure 14. VC thermal resistance performance compared to a solid heat spreader. VC features, black powder and heater of 5 mm x 5 mm

The same previous cases are performed using a VC with red powder now and the results are in Figure 15. This is effectively changing the capillarity; the results show none of the cases outperformed the SHS. *Thus the capillarity is critical in the VC performance*.

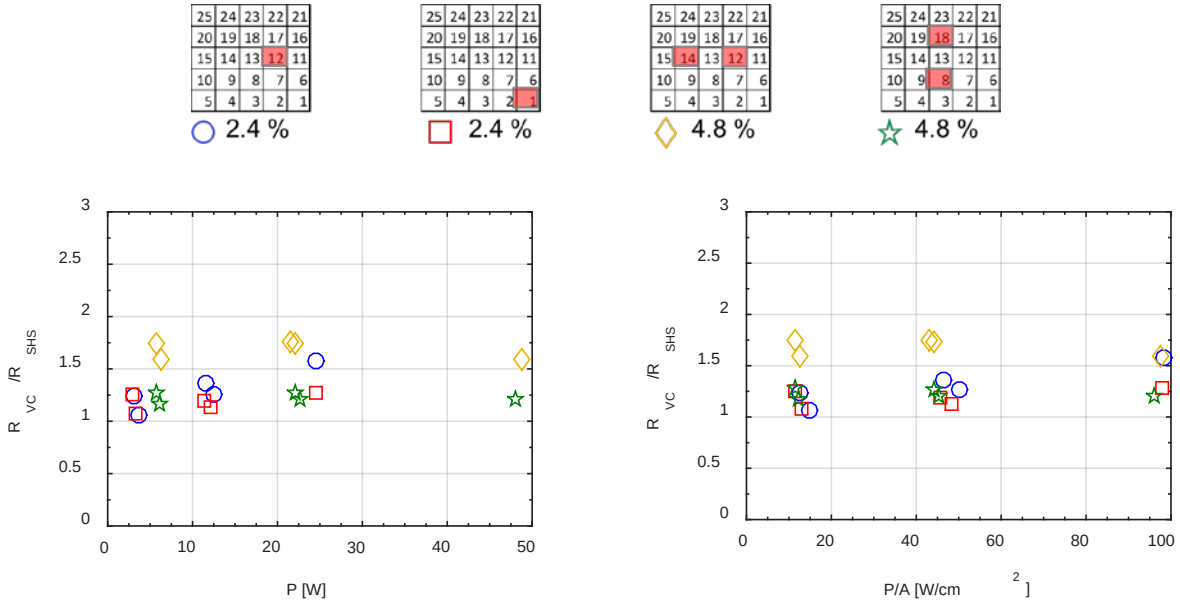

Figure 15. VC thermal resistance performance compared to a solid heat spreader. VC with Red powder, heater of 5x5.

The thermal resistance of the SHS experiments is compared to the solution of an analytical model developed by Muzychka et al [Muzychka et al, 2003]. The analytical solution is programmed in Mathematica and solved; acknowledging the model may differ from actual measurements, the ratio $R_{SHSexp}/R_{SHSmodel}$ results in an average value of 3 with a maximum of 5 and a minimum of 1.5. The experiments were consistently having larger thermal resistance. Therefore Muzychka's model is used here only as a tool to see trend rather than trying to calculate the SHS thermal resistance. Using the model, we see a R_{SHS} reduction of 2.9% for a convective heat transfer coefficient value "h" increase of 200%, this is a very small change on R_{SHS}. The change in thermal resistance should be related to non-uniformity temperature due to the spreading resistance; for a solid heat spreader experiencing no spreading resistance the thermal resistance must not depend on convective heat transfer coefficient "h". The SHS thermal resistance is not function of the power neither from the operating temperature. The SHS thermal resistance increases by decreasing the thickness "t" in the form of $R_{SHS} = 0.78\left(\frac{1}{t}\right) + 0.212$ this effect is caused by the spreading resistance the solid heat spreader presents.

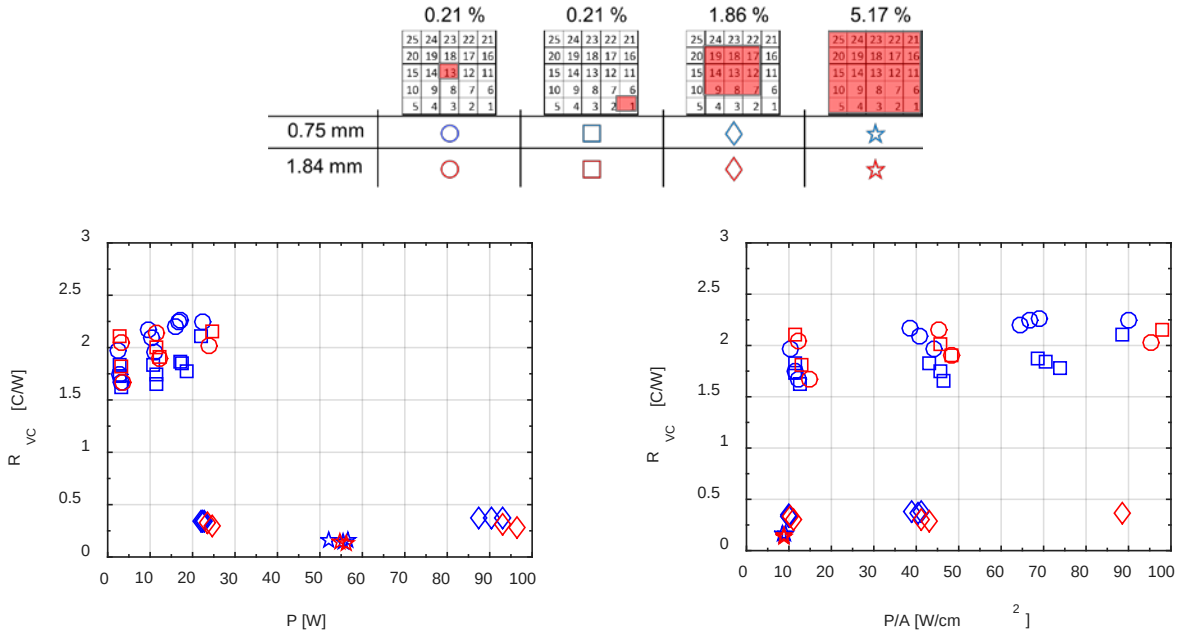

Figure 16. Vapor core thickness effect on the VC thermal resistance. Same powder (Red) and heater size (5x5) for all cases. % numbers indicate the value of the fraction $A_{heaters}/A_{VC}$*100

The effect of the vapor core is explored by looking at the thermal resistance measurements from the two VCs with same powder but different vapor core thickness. We do not have experimental data for a SHS with thickness equivalent to the VC with 0.75 vapor core thickness, thus the conclusions for the vapor core thickness effect are based on the VC thermal resistance values only. Figure 16 shows the comparison for the two tested VCs for different configurations of active heaters as depicted at the top of

the figure. *The thermal resistances for both VCs are not significantly different thus we can infer no effect of the vapor core for the tested VCs*.

The heater size should have an effect on the VC thermal resistance and this is clear in Figure 17 where the thermal resistance is plotted for different cases of heater size and for different cases of active heaters (all cases are centered). The case of one active heater at the center better illustrates the increase of the thermal resistance due to the heater size. This should be due to the fact that the vapor and liquid have to travel longer to the condenser and hot region respectively, thus the resistance to spreading is larger. *Therefore, the smaller the heat source the larger the spreading resistance*.

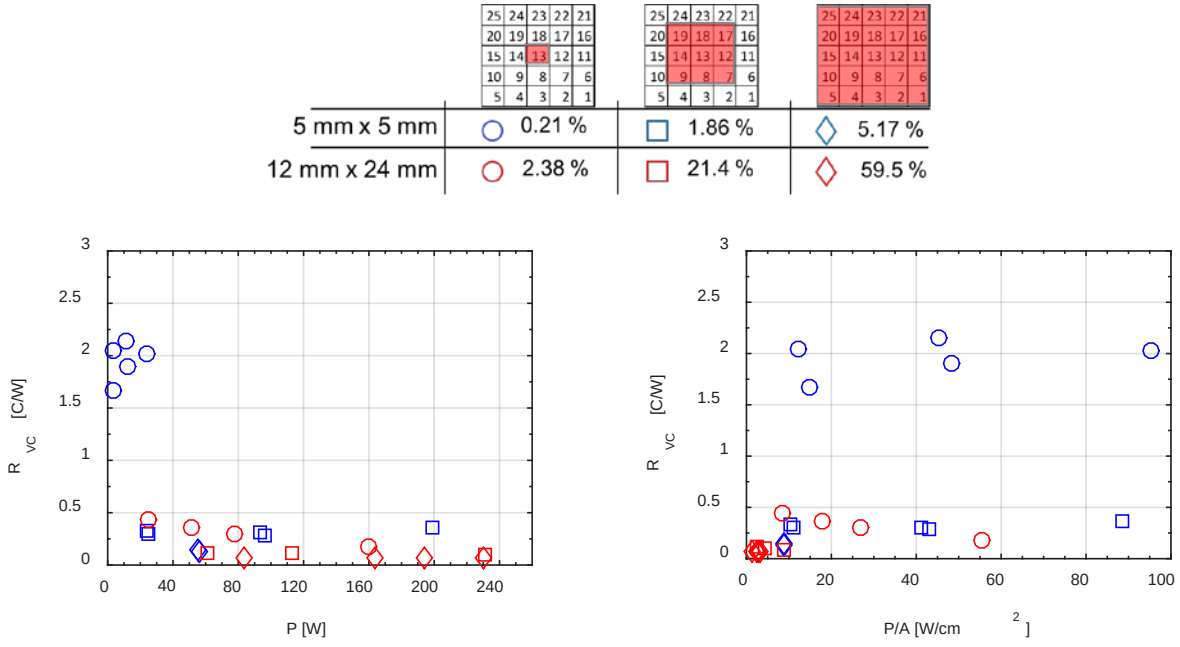

Figure 17. Effect of heater size

An interesting outcome of the experimental data analysis is seeing superposition on the VC (red powder, 5.4 mm thick). Superposition is true in solid bodies where heat transfer is purely by conduction. It was not expected to see superposition in a VC however we notice this effect. The superposition in the VC measurements may be because heat is being transferred by conduction thus the VC is not taking advantage of the convection due to vapor moving in the VC core, this can be the reason why the red powder VC has a lower performance than the SHS; appendix A has selected plots illustrating the superposition effect.

5 Analysis

Here we describe different numerical models used to calculate the thermal resistance using assumptions on the boundary conditions and simplifying the governing equations. The easiest method

to calculate the thermal resistance is the use of a 1-D conduction problem where the thermal conductivity is the same as those of the different VC layers. The 1-D conduction thermal resistance does not consider spreading resistance, the equation is

$$R = \frac{t}{kA} \qquad \text{Eq. 4}$$

Where *t* is the thickness [m], *k* is the thermal conductivity [W/mK], and *A* is the area normal to the heat flow direction [m^2]. First order bounds are obtained by solving this equation for an area similar to the VC (144 mm x 84 mm), variable thickness, and considering the thermal conductivity of: copper, water vapor, and water liquid. The heat source is assumed the same area as the VC in order to have a 1-D problem. The solutions are the solid lines in Figure 18. These lines have the highest and lowest thermal conductivites therefore, any experimental result from the VC should fall within these bounds.

A higher order approximation is to include the spreading resistance effect, using Kennedy's curves for a spreading factor and using the equation

$$R = \frac{H}{k\pi a} \qquad \text{Eq. 5}$$

Where *H* is determined from Kennedy's curves [found in Tummala et al, 1997], "*a*" is the equivalent radius of the rectangular heat source. The thermal resistance has a smaller slope meaning the thermal resistance is less dependent on the solid heat spreader thickness (Figure 18). Also, the spreading resistance increases when the heat source decreases, this is the effect seen in Figure 17.

Another iteration to better reflect the thermal resistance calculation is the use of layers with different thermal conductivities,we will call this method "segmentation". This segmentation method has a more realistic representation of the VC. An assumption made is thermal spreading occurs only in the layer in contact with the heat source; this is an assumption made to better represent the VC while still having an equation simple enough to solve without diving in the actual complex processes occurring in the VC. The thermal conductivities for the solid layers are constant and for copper material, the thermal conductivity for the wick is calculated using the relation for sintered powder [Wei and Sikka, 2006] shown below

$$k_{wick} = k_s \left[\frac{2 + \frac{k_l}{k_s} - 2\epsilon\left(1 - \frac{k_l}{k_s}\right)}{2 + \frac{k_l}{k_s} + \epsilon\left(1 - \frac{k_l}{k_s}\right)} \right] \qquad \text{Eq. 6}$$

Furthermore, the vapor core thermal conductivity k_v is determined using [Prasher, 2003]

$$k_v = \frac{h_{fg}^2 P_v \rho_v t_v}{12 R \mu_v T_v^2} \qquad \text{Eq. 7}$$

Where h_{fg} is the latent heat of vaporization [J/kg], P_v is the vapor pressure [Pa], ρ_v is the vapor density [kg/m3], t_v is the vapor core thickness [m], R is the gas universal constant [J/kgK], μ_v is the vapor viscosity [(N-s)/m^2], and T_v is the vapor core temperature [K]. The thermal resistance is calculated using this method and thermal conductivities and assuming the heat source is at the center, Figure 18 shows two points (black) one for each heater size and using a thickness of 5.4mm corresponding to the experimental solid heat spreader thickness.

The VC manufacturer reported an "evaporator resistance" of 0.2 [(C-cm^2)/W], however care should be taken in that the manufacturer claimed value differs in definition since they report the "evaporator resistance" as the maximum temperature difference at the evaporator side divided by the applied power (200 W) to the VC. The maximum temperature difference at the evaporator side is given by one spring loaded thermocouple at the hottest location, and a thermocouple on the opposite corner at the same evaporator side. Thermacore reports their testing consisted of a heat source of 25.4 mm x 25.4 mm. The "evaporator resistance" is plot as the green marker, Figure 18 tells us that the VC evaporator resistance is equivalent to a Cu solid being heated by a heat source the same size of the base. Using the thermal resistance definition (Eq. 5) and the heat source of 25.4 mm x 25.4 mm considering spreading we can see the VC should have a larger thermal resistance than the "evaporator resistance" given by Thermacore.

Figure 18 include the thermal resistance experimental measurements for the VC with a single heater at the center and using the two different heart sizes. The measured value differs by a factor of 10 and 5 respect to the calculated value by the method of segmentation and spreading respectively. *Thus, although the models are simplified and quick to solve there is a factor to correct for when using these models. Further work is needed to determine if the factors are consistent for different VC thicknesses*.

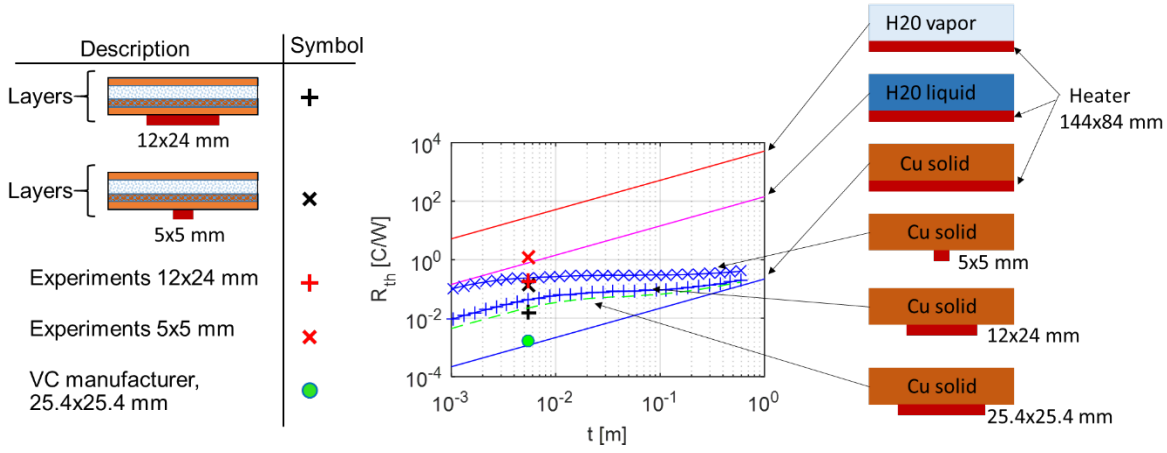

Figure 18. Thermal resistance methods comparison and experimental data

Revisiting the wick thermal conductivity in the segmentation method we find that a correlation given by Chi [Wei and Sikka, 2006] is the most commonly used for VCs.

$$k_{wick} = \frac{\pi}{8}\left(\frac{r_c}{r_s}\right)^2 + \left[1 - \frac{\pi}{8}\left(\frac{r_c}{r_s}\right)^2\right]\left[\frac{k_l k_s}{\epsilon' k_s + k_l(1-\epsilon')}\right] \quad \text{Eq. 8}$$

Where

$$\epsilon' = \frac{\epsilon}{1 - \frac{\pi}{8}\left(\frac{r_c}{r_s}\right)} \quad \text{Eq. 9}$$

Where k_l is the liquid thermal conductivity [W/mK], k_s is the solid thermal conductivity [W/mK], r_c is the contact radius [m] here it is assumed to be the porous radius, and r_s is the particle sphere radius [m]. The thermal conductivity for the wick is calculated using the values in Table 3 for the models from Maxwell, and Chi.

Table 3. Parameter values used for the thermal conductivity correlations.

Correlation	Parameters
Maxwell	k_l=0.58; k_{cu}=380; ε=0.6
Chi	k_l=0.58; k_{cu}=380; ε=0.6; r_s=92*10^{-6}; r_c=46*10^{-6}

The resulting thermal conductivity and the thermal resistance are reported in Table 4

Table 4. Thermal conductivity and thermal resistance results using the two different thermal conductivity models.

Correlation	k_{wick}	R_{th} (simple model)	
		A_h: 5x5 mm	A_h: 12x24 mm
Maxwell	95.4	0.1276	0.0132
Chi	38.0	0.1289	0.0145
% difference		1	9.0

The percentage difference in thermal resistance is small thus no significant deviation on the results from Figure 18 is expected by using Chi correlation.

5.1 Heat transport limitations

Vapor chambers are also known as flat heat pipes, both of them use: wick to move the fluid, a change of phase from liquid to vapor to spread the energy and the vice versa process to recover the fluid out of the vapor. The difference is heat pipes are mainly used to transport heat from location “A”

to location “B” while vapor chambers are used to spread energy from a concentrated region to a larger region.

The heat pipe maximum performance is limited by: viscous limit, sonic limit, entrainment limit, capillary limit, and boiling limit.

The viscous limit relates to low temperatures where the fluid is so viscous that it offers a large resistance to fluid movement thus starving fluid to the hot area occurs, this limit is given by:

$$\dot{Q}_{viscous} = \frac{D_v^2 h_{fg} P_v \rho_v}{64 \frac{\mu_v}{\rho_v} l_{eff}} \quad \text{Eq. 10}$$

Where $\dot{Q}_{viscous}$ is the heat rate vapor limit [W], D_v is the hydraulic diameter for the vapor core cross sectional area [m^2], and l_{eff} is an effective distance [m]. The sonic limit occurs when compressibility effects are considerable (M > 0.2) and it may create a sonic wave limiting the fast transport of vapor, this limit is given by:

$$\dot{Q}_{sonic} = 0.47 A_v h_{fg} \sqrt{P_v \rho_v} \quad \text{Eq. 11}$$

Where $\dot{Q}_{sonic}$ is the heat rate sonic limit [W], A_v is the vapor core cross sectional area [m^2]. The entrainment limit describes a process where the stress at the vapor-fluid interface is so large that droplet are generated and enter the vapor region, the result is the amount of liquid is reduced thus starving the hot region from cool fluid. This limit is given by:

$$\dot{Q}_{entrain} = A_v h_{fg} \sqrt{\frac{\rho_v \sigma}{2 r_c}} \quad \text{Eq. 12}$$

Where $\dot{Q}_{entrain}$ is the heat rate entrainment limit [W], σ is the fluid surface tension [N/m], and r_c is the contact radius [m]. The capillary limit occurs when the capillary force driving the liquid is smaller than the fluid resistance to move through the porous medium thus causing liquid starvation to the hot area, this limit is given by:

$$\dot{Q}_{capillary} = \frac{\frac{2\sigma}{r_c} - \rho_l g l_t \sin\varphi}{\frac{l_{effc} \mu_l / \rho_l}{A_w K h_{fg}} + 8 \frac{\mu_v / \rho_v}{h_{fg} \pi \left(D_v / 2\right)^4}} \quad \text{Eq. 13}$$

Where the subscript “l” indicates properties for the liquid, g is the gravity [m/s^2], φ is the inclination angle, l_{effc} is an effective capillary length [m], A_w is the cross sectional area of the wick [m^2], K is the wick

permeability [m^2]. The boiling limit results when the temperature at the hot surface is larger than the liquid boiling temperature thus generating bubbles, while bubble nucleation increases the VC power dissipation capability it can generate bubble large enough to get stuck in the wick. Once a large bubble forms and sits in the wick, it will prevent the liquid from reaching to the hot are thus causing the VC to fail, this limit is given by:

$$\dot{Q}_{boiling} = k_l \left[\frac{\left(1+\frac{k_s}{k_l}\right)-\varepsilon}{\left(1-\frac{k_s}{k_l}\right)+\varepsilon}\right]\frac{3.06\sigma T}{\rho_v h_{fg}\delta}\frac{}{t_w} \qquad \text{Eq. 14}$$

Where $\dot{Q}_{boiling}$ is the heat rate boiling limit [W], k_s is the solid thermal conductivity [W/mK], ε is the wick porosity, T is the VC operation temperature [C], δ is the thermal layer thickness [m] the typical value is 25x10^{-6} m, t_w is the wick thickness [m].

Using Eqs. 10-14, the fluid properties, and the dimensions of the experimental VC we plot the limits with respect to the VC operation temperature. *Figure 19 shows the capillary limit is the mode restricting the maximum performance*.

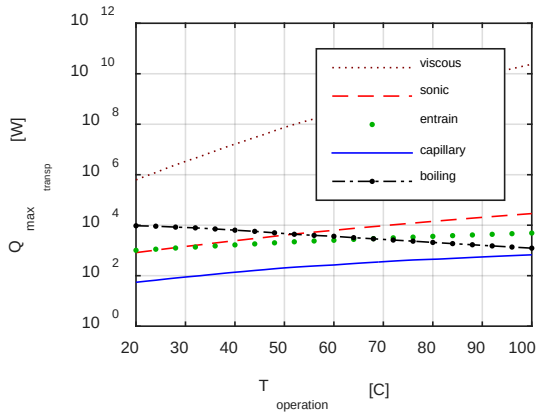

Figure 19. Heat transport limits for a heat pipe using the VC geometric parameters

In Figure 19, we assumed a value of 1x10^{-11} m^2 for the permeability since the VC manufacturer did not provide it. An extended analysis is shown in Figure 20, it is a sensitivity analysis of the maximum heat transport to the permeability value. The permeability range considered in the plot is 10^{-8}-10^{-12} m^2 this includes most permeability values found in commercial and research VCs.

Our VCs worked on the 50-60 C operating temperature and they are designed to dissipate 200 W; conversations with Thermacore resulted in communicating the VC is may be able to dissipate 300 W before hitting any limit. *The 200-300 W dissipation for 50-60 C operating temperature is reflected in the capillary limit calculated using 10^{-11} m^2 as the permeability value; the heat transfer capillary limit*

indicates permeability values smaller than 10^{-10} m^2 have significantly less effect. We consider the VCs have permeability of 10^{-11} m^2.

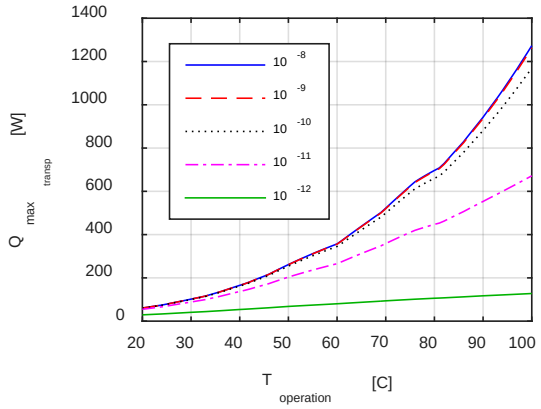

Figure 20. Heat pipe capillary limit at different permeability *K* values

6 Thermal resistance calculation

We take as an exercise to define three methods to calculate the VC thermal resistance (Figure 21) and analyze advantages and disadvantages.

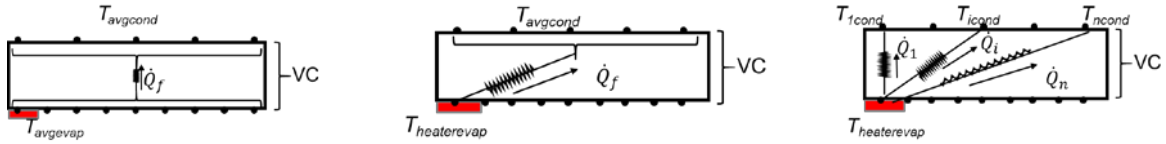

a b c

Figure 21. Methods to calculate simplified thermal resistance

The first method R_{m-m} takes the average temperature at the VC evaporator side and the average temperature at the condenser side; the temperature difference is divided by the total power passing through the vapor chamber (Eq. 15). This is a quick method to estimate thermal resistance but it fails to detect the maximum temperature at the evaporator side. It is important to consider the maximum temperature at the evaporator side to ensure the VC has a thermal resistance capable of cooling down that maximum temperature.

$$R_{m-m} = \frac{\left(T_{avgevap} - T_{avgcond}\right)}{\dot{Q}_f} \qquad \text{Eq. 15}$$

The second method R_{l-m} considers the maximum temperature at the evaporator side and subtract it from the average temperature at the condenser side; dividing the temperature difference by the power through the VC defines the thermal resistance (Eq. 16). This is the common method to calculate VC thermal resistance; however considering the average temperature at the condenser side may introduce errors if the temperature measurement points do not capture the temperature profile properly (e.g. they are located within the same isothermal band that may be present in the VC condenser side)

$$R_{l-m} = \frac{\left(T_{heaterevap} - T_{avgcond}\right)}{\dot{Q}_f} \quad \text{Eq. 16}$$

The third method is to consider a discrete domain at the condenser side and the maximum temperature at the evaporator side along with the heat transfer through each connecting paths (see Figure 21). This method is defined with Eq. 17.

$$R_{l-l} = \frac{1}{\sum_{i=1}^{n} \frac{1}{\left(T_{icond} - T_{heaterevap}\right)} \dot{Q}_i} \quad \text{Eq. 17}$$

where

$$\dot{Q}_f = \sum_{i=1}^{n} \dot{Q}_i \quad \text{Eq. 18}$$

Where $\dot{Q}_f$ is the total heat dissipated by the VC and $\dot{Q}_i$ is the heat transfer through each path; $\dot{Q}_i$ is calculated with the Eq. 19

$$\dot{Q}_i = -kA_i \frac{dT}{dn} \quad \text{Eq. 19}$$

And the thermal resistance along this path is

$$R_i = \int_0^N \frac{dn}{kA_i(n)} \quad \text{Eq. 20}$$

The maximum temperature at the evaporator side is considered a point, and the temperature on the condenser side is consider to be discrete across the grid and uniform within each grid element. Solving Eq. 20 requires to know how the area changes, for each element "*i*", with distance n; the area change is represented with a second order polynomial (Eq. 21)

$$A_i = a_i n^2 + b_i n + c_i$$ Eq. 21

This method assumes the heat source is infinitesimally small compared to the VC condenser side; the assumption of a single point at the evaporator side brings the problem of singularities in the integral calculation (*A(x=0)=0*), to avoid this problem the problem is entered with a value of $t\text{-}\delta=t_{VC}$ where δ is a small thickness (1 nm), t_{VC} is the VC thickness, t is a thickness calculated as $t=t_{VC}+\delta$. During the calculation the volume elements are considered to have different thermal conductivities representing the copper solid layers, the wick layer, and the vapor core layer (Figure 22); these thermal conductivities are calculated using the Eqs. from Section 5.

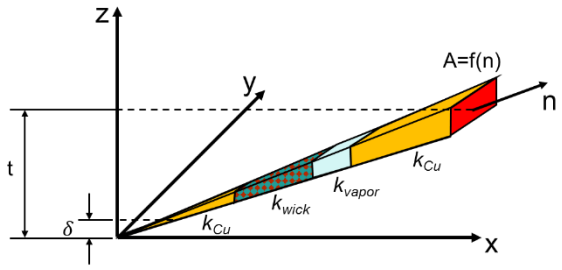

Figure 22. Schematic showing the different segments in a differential volume element. Z=δ corresponds to the base of the VC, δ is the removed thickness to avoid singularities

Assuming a hot element is at the center of the VC evaporator side, the local thermal resistance for each of the volume elements is shown in Figure 23 where we can see the minimum local resistance is at the top of the hottest element. The local thermal resistance is inversely proportional to the grid size since the element volume is smaller for larger grids.

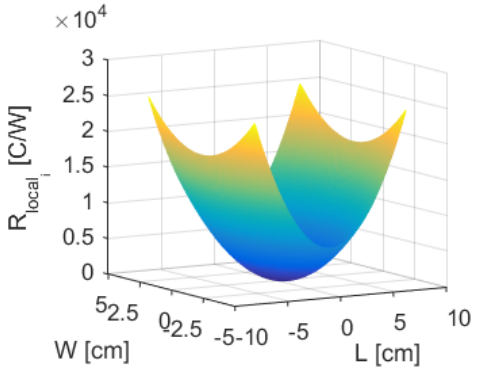

Figure 23. Local thermal resistance for a mesh of 201 point on x and 201 on y.

The toal VC thermal resistance is independent of the grid size and it is calculated as shown in Eq. 22.

$$\frac{1}{R_{VC}} = \sum_{i=1}^{n} \frac{1}{R_{local_i}} \qquad \text{Eq. 22}$$

This method has its complexity that leads us to think of it as an alternative to the simpler methods. It is necessary to perform an error analysis on these methods to quantify the differences between each of the methods.

7 Simulations

The VC numerical simulation results from using Fluent to solve a model considering spatial (3D) and transient effects. The model uses: phase change as a boundary condition, user defined functions (UDF), and parallelization of the code to reduce the computational time from 5 days to 1 day.

The model was developed during the early phases of the project and the case scenarios considered were set based on potentially interesting configurations such as having simultaneously active two high power component and eight low power components, other cases were having one high power component and four low power component. The components distribution is shown by the solid black lines on top of Figure 24b.

A second model is developed to simulate the liquid flow through the wick (porous medium); the model is solved using the two-point flux-approximation (TPFA) method [Arnes et al. 2007]. This model does not include two phase change nor heat transfer effects; it works as a second point of validation for the flow in the wick results from the Fluent model.

Figure 24 shows the simulations results using both models for the case of two high power components and eight low power components. This is a symmetric configuration thus finding the highest temperature at the center of the high power components is expected. The maximum vapor velocity reaches values of 9 m/s and it is aligned with the direction of the long axis of the high power components. The velocity results in M≈0.03 (where M is the Mach number *M=u/c*, *u* is the vapor velocity and *c* is the sound speed in the medium 300 m/s assumed), *since M<0.2 fluid compressibility effects may be neglected thus no sonic limit is reached within the VC*. The symmetry of the problem results in symmetry in the vapor velocity distribution, however without the model it is not clear where the maximum velocity will occur for different symmetric configurations. The liquid velocity in the wick (max velocity 1.4×10^{-3} m/s) is determined with the model*, the difference in fluid maximum velocities in the vapor and in the liquid reaches up to four orders of magnitude; this may be enough to consider entrainment, due to shear stress, of liquid from the liquid into the vapor*. In order to determine the likelihood of entrainment, it is necessary to do in the future a linear stability analysis of the vapor-liquid interface.

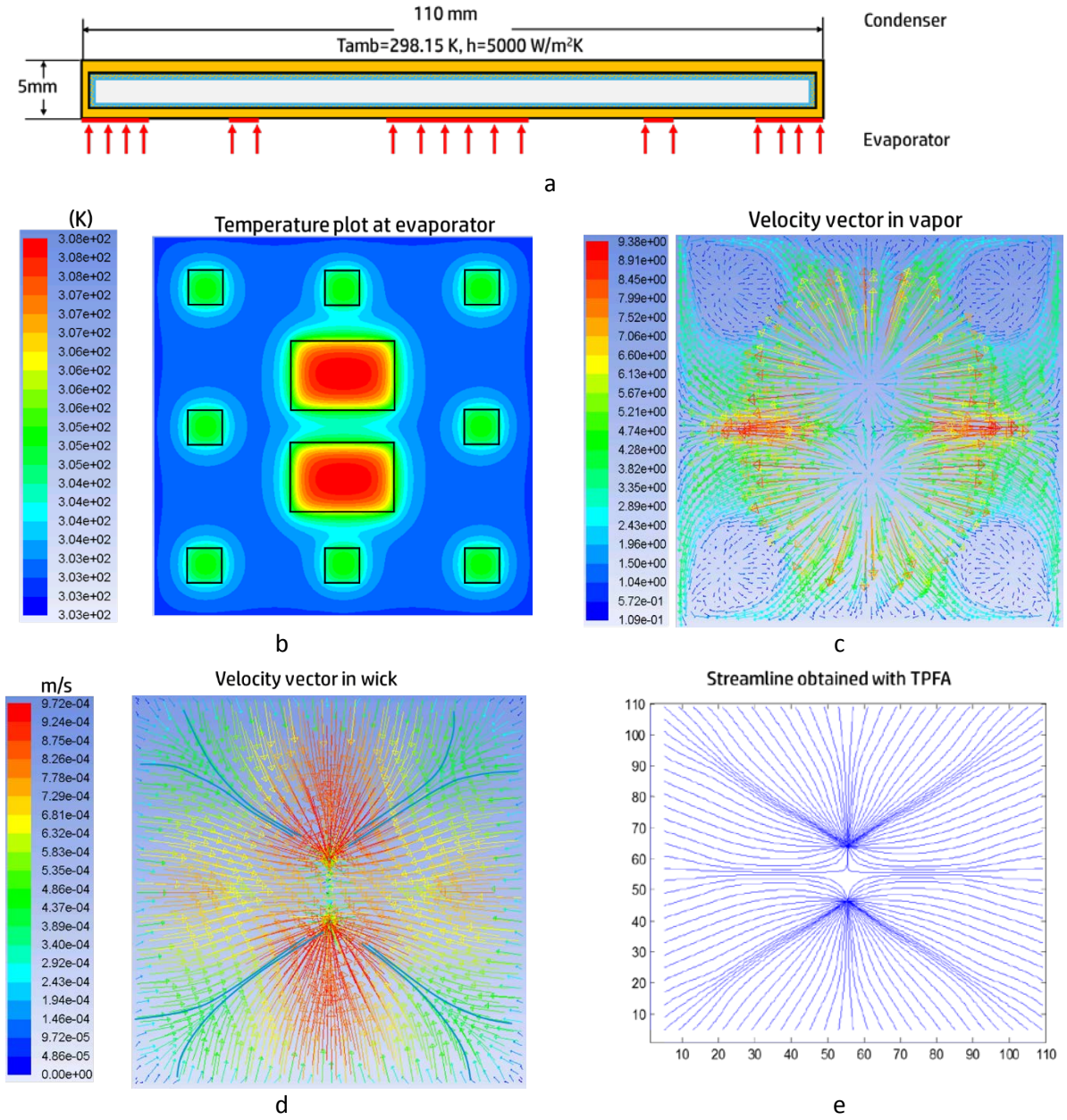

Figure 24. Simulations: CFD model for a) boundary conditions, b) Temperature profile, c) Vapor velocity, d) liquid velocity in the wick; TPFA model e) liquid velocity in the wick

The TPFA is a simplified model to determine the liquid flow velocities (maximum velocity 6.3×10^{-4} m/s) and streamlines in wick. The velocity profiles show similar features comparing the TPFA and the VC full model however the maximum velocity magnitude differs by an order of magnitude. This leads to *consider the TPFA as a simplified tool to be used qualitatively in determining where the fluid capillary force could fail*. The maximum velocity is related to the capillary limit in the VC thus having a reliable estimate is important to determine the capillary limit.

Figure 25 shows the results for two additional different configurations of heat sources locations. *It is clear the heat source location (power map) impacts the fluid distribution in the vapor and wick, and power magnitude and power density will affect the fluid velocity magnitude*. The VC and TPFA tool are valuable in determining the possible VC failure due to capillarity limit.

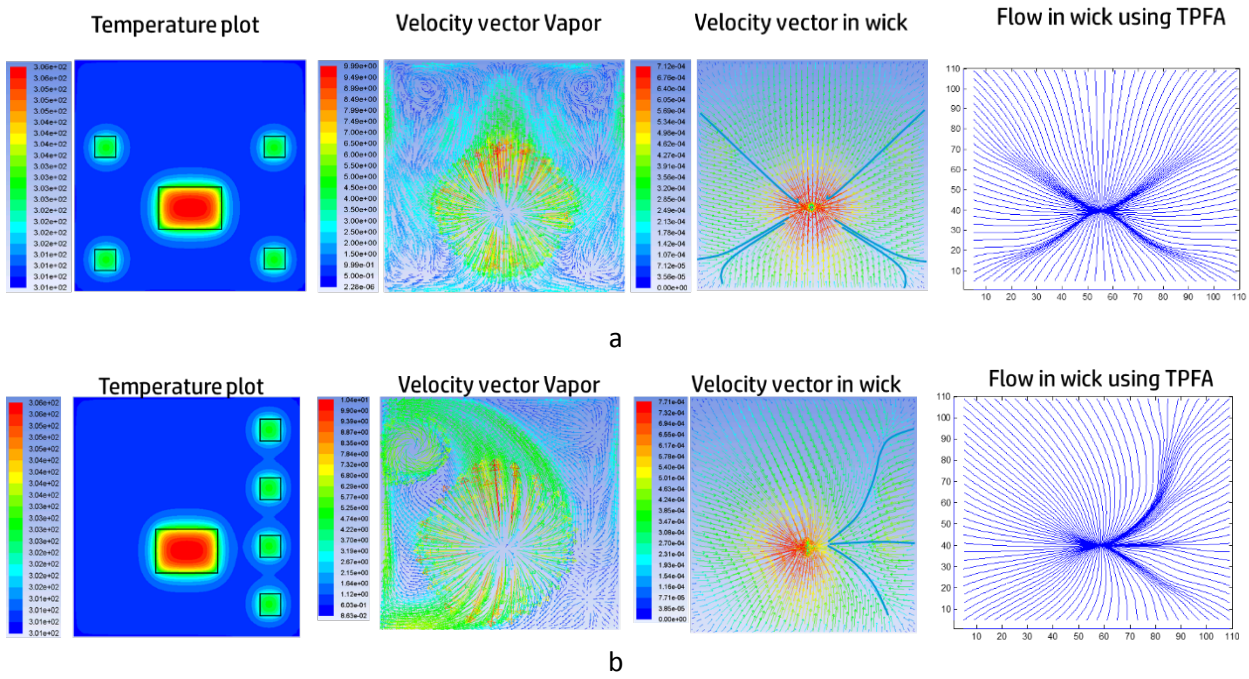

Figure 25. Heater location effect on the temperature and flow profiles. a) Low power components surrounding high power component; b) Low power components on one side of the high power component

7.1 Simplified CFD

A set of CFD simulations are performed to compare different modeling techniques representing vapor chamber devices. The goal of these methods is to simplify the modeling of the cooling devices. The study results in new recommendations for VC modeling after comparing the CFD results with experimental data.

This study uses mentor Graphics' FLOTHERM software package and it simplifies the VC CFD model. The simplifications enter as boundary conditions for the VC interaction with other TTV components (e.g. cold plate, heater blocks, etc.). The simplified VC model consists on the outside of two main parts: condenser plate and outer shell. The condenser plate sits on top of the outer shell, creating a hollow space. Inside this area is the wick and vapor structure. The bottom of the outer shell is the evaporator face in contact with the heater blocks. A detailed description of the model is given in the PI-HPE internal report [Ferrer 2016]. Table 5 provides details of the CFD simulations, The CFD model and the experimental data define model parameters that best represent the VC.

Table 5. Study case for simplified CFD model.

CFD Study	Column Header	Description
CFD Study #1	Solid Metal Base	Simulate complete vapor chamber as a solid block material (metal). Materials tested: copper and aluminum.
CFD Study #2	Vendor Model 1 (VM 1)	Simulate complete vapor chamber as one solid block with different effective isotropic and orthotropic conductivities, typically used for system simulations: • Isotropic: o k_{eff} (W/mK) = 2000, 3000 and 5000 • Orthotropic: o k_{eff} (W/mK) = 3000 (in-plane) and 385 (through)
CFD Study #3	Vendor Model 2 (VM 2)	Simulate each vapor chamber layer (outer shell, condenser plate, wick and vapor) as individual solid blocks. The wick and vapor layers modeled as solid with VC vendor recommended effective conductivity: • Wick k_{eff} (W/mK) = 40 • Vapor k_{eff} (W/mK) = 50,000
CFD Study #4	Detailed VC Model (VC 1)	Vapor chamber modeled in more detail (each layer as solid and pillars included). Different levels of effective thermal conductivity for the wick and vapor layer: • Wick k_{eff} (W/mK) = 40, 30, 20, 10, 8, 6, 4, 3, 2 and 1 • Vapor k_{eff} (W/mK) = 50k, 25k, 10k, 5k, 1k, 800, 600, 400, 300, 200 and 100

Results and analysis from the CFD model are presented in the internal report PI-HPE [Ferrer 2016]. The final values selected are within +/- 5% difference from the experimental results. We can see from this analysis that both the wick and vapor effective conductivities need to be higher as the power density increases, in other words the VC thermal conductivity variable should have a functional form with power. *It is this behavior that we recommend CFD software packages should include in their modeling options so users can import a "heat flux-thermal conductivity" function to a single "smart part" or object. We also recommend vapor chamber vendors to performed testing and publish this type of thermal performance data, and even some kind of industry testing standards could be created so the same testing procedure and reporting is used no matter the vendor or supplier*.

7.2 VC isothermal factor

One of the benefits of a vapor chamber is the ability to spread the heat efficiently across the device, which results in a uniform temperature distribution across the condenser face. This "isothermal" effect allows better utilization of heat sinks and other cooling devices attached at the top of the vapor chamber, improving the thermal performance of the complete cooling solution for electronic devices. It is therefore important to evaluate how well the CFD method captures this attribute of vapor chambers. The isothermal factor can be calculated using the following equation:

$$\propto = \frac{\sigma_{es}}{\sigma_{cs}} \qquad \text{Eq. 23}$$

Where σ_{es} is the standard deviation of the thermocouple data at the evaporator face and σ_{cs} is the standard deviation of the thermocouple data at the VC condenser side.

Typically, the temperature variability at the condenser face is much smaller than the temperature variability at the evaporator face for vapor chamber devices (this is their "isothermal" benefit). Therefore, the isothermal factor will usually be higher than 1, and the higher the factor the better performance it should give. An extensive discussion on the isothermal factor is found in supported documents [internal report: Ferrer, 2016].

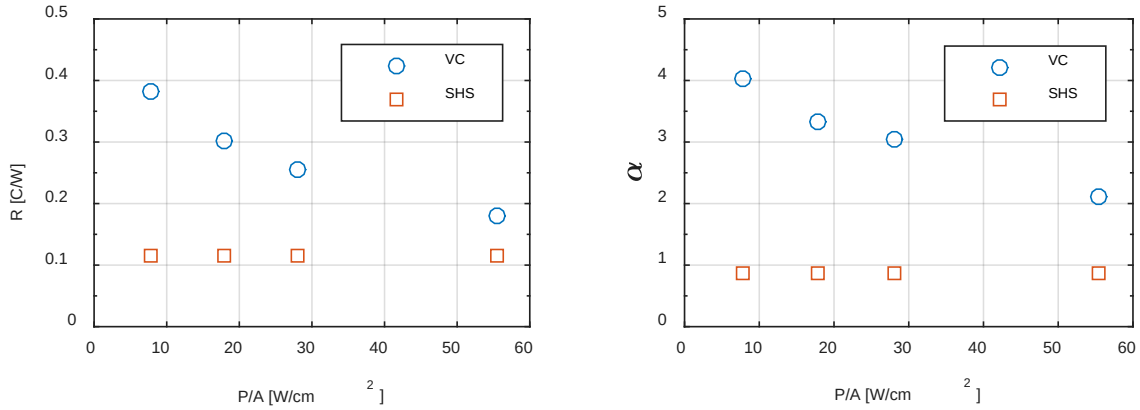

Figure 26. CFD VC simulations calculated for the isothermal factor

It is interesting that while the total thermal resistance reduces with higher heat flux the isothermal factor also reduces (see Figure 26, Ferrer 2016). This behavior is understood since as the effective thermal resistance increases with a reduction in heat flux applied the temperature distribution at the condenser is more uniform, which results in a higher isothermal factor

8 Conclusions:

Using vapor chambers to cool multiple chip modules is viable as long as several factors are kept on mind. The selection of a vapor chamber should be based not only on the thermal resistance value but also in a series of parameters such as: heat location, power, power density, and temperature uniformity at the condenser side. General guidelines are that VC performs better for: high power, power density, off center or asymmetric heat sources.

A new metric is proposed to include in the VC selection, this metric accounts for the temperature uniformity at the VC condenser side. This metric is useful in the larger picture of energy savings since it

is a metric to indirectly calculate how much cooling energy will be used by the pumping device e.g. fan or liquid pump.

The limitations from a vapor chamber can be reached for under certain conditions e.g. thin VC vapor cores are more likely to reach the sonic limit; high power or high power density are more likely to reach the boiling limit; poor wick permeability is likely to run into capillary limit. In the current experiments, capillary limit is the leading limitation; this limit is the most common on VCs. The capillary limit is the dominant parameter in the VCs studied in this work. Therefore the VC design has to consider careful attention to the wick permeability and design. We developed two numerical models to determine the flow in the wick, such models can be used to design vapor chambers wick layer for a given power map. The power map may determine if a VC is better alternative than a SHS. 1D models work as a quick approximation to determine VC thermal resistance but they include large errors therefore more refined models should be used.

Experimental measurements here reported provide data for numeric models, the data can be used for future models validation as well. The data includes three different VCs, a SHS, and a range of combination of heater locations. Similarly, alternative methods to numerically calculate the thermal resistance are introduced, such methods can be used when refined calculations are desired.

Additional to the conclusions from the VC study, we developed and improved a wet bench to test the performance from liquid cooled systems (e.g. cold plates, VCs, Heat pipes, server's liquid cooling loops etc.). The wet bench is capable of controlling flow rate and fluid temperature, it has sensors to monitor flow resistance and temperature resistance from the device to be tested. New instrumentation is developed as well; this instrumentation should be used for future testing, the TTV has tremendous flexibility and range of operation. The software interface developed for the TTV is such that it is a valuable tool to do programmable testing.

9 Appendix A

9.1 Superposition

The temperature distribution can be estimated using the superposition principle. The superposition can be defined with the following equation

$$\theta_{superposition}(x,y,z) = \sum_{i=1}^{n} \theta_i(x,y,z) \qquad \text{Eq. 24}$$

Where $\theta = T - T_{ref}$, T is the temperature, T_{ref} a reference temperature, $\theta_{superposition}(x,y,z)$ is the spatial temperature distribution when multiple heaters are simultaneously active; $\theta_i(x,y,z)$ is the temperature distribution of the single active "*i*" heater, *n* is the total number of simultaneously active heaters. The superposition applies when the heat transfer is dominated by thermal conduction; during our experiments we tested for superposition and found the superposition is present for the VCs with red powder (we did not complete the testing for the black powder to investigate if superposition is present). Experiments consisted of running experiments with single active heaters and then adding arithmetically the results form the single active heaters. An example is shown in Figure 27, where experiments are performed having one single active either 17 or 9, later the experimental measurements are arithmetically added to obtain the series "Added" in Figure 27a; the "Added" series is then compared to another experiment where the heaters "17" and "9" are simultaneously active (Figure 27b). It is clear the "added" series and the experimental data with simultaneously active heaters strongly correlate.

Figure 27 shows the measurements from two experiments running different one single active heater (17 and 9). The results from each experiment is added arithmetically and then plotted as shown by the series "Added" in Figure 27.

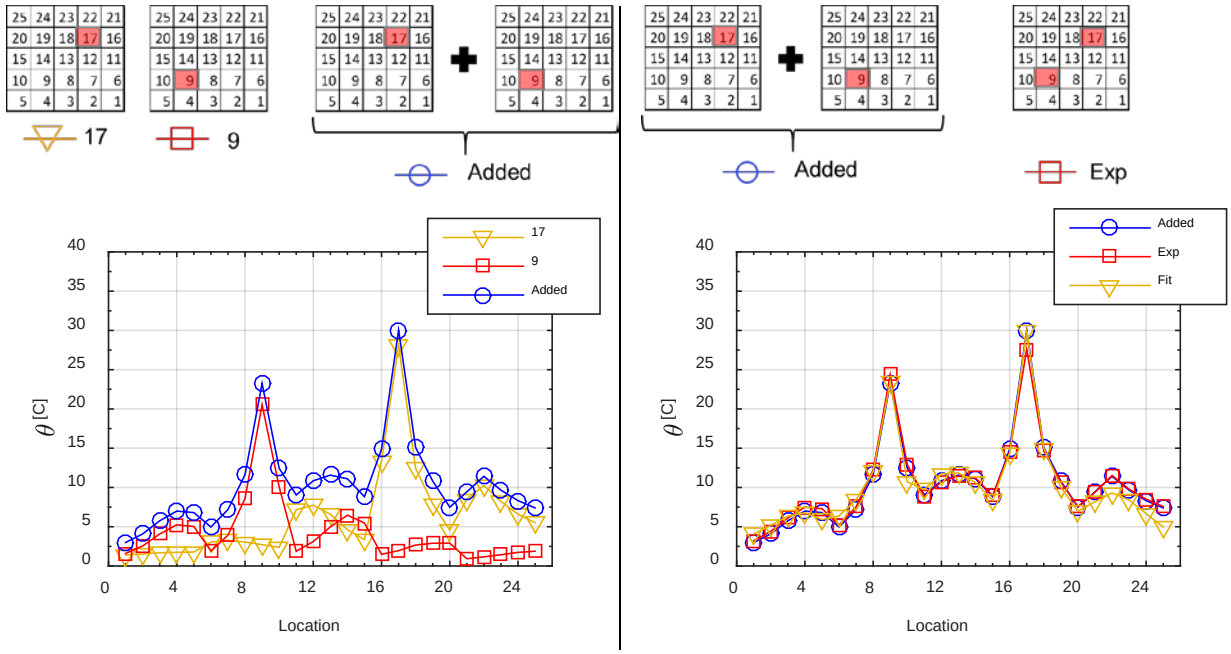

a | b

Figure 27. Temperature superposition effect on the VC evaporator side: a) Experimental data for single active heaters and arithmetic addition of the same data; b) Experimental data for two simultaneously active heaters and comparison to the arithmetic addition of the single active heaters and a fit line to predict the temperature distribution

The "Fit" series is the result of using an exponential function to describe the temperature distribution due to each of the active heat sources, this is the result from using an equation of the form

$$\theta = \frac{1}{a_1\sqrt{2\pi}} e^{\frac{1}{2}\left(\frac{x}{b_1}\right)^{n_1}} + \frac{1}{a_2\sqrt{2\pi}} e^{\frac{1}{2}\left(\frac{x}{b_2}\right)^{n_2}} \qquad \text{Eq. 25}$$

The fitting constants "*a*", "*b*", and the exponent (*n*) are obtained after fitting each term to the single active heat source (sources 1 and 2, the numerals used in Eq. are generic references, they do not refer to location) temperature profile. Such functional form neatly follows the experimental data on the VC evaporator side as shown in Figure 27b above. The condenser side has significantly more noise and it is necessary to use a different functional form for a fitting (in this work we did not get to the point of trying different functions thus Figure 28 does not include the Fit curve

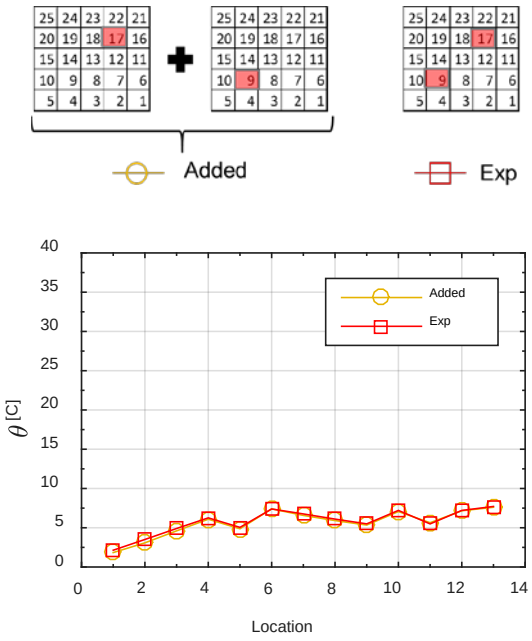

Figure 28. Superposition at the condenser for the active heaters 17 and 9

10 References

Arnes J.E., Gimse T., Lie K., 2007, ”An introduction to the numerics of flow in porous media using Matlab” pp. 265-306.

Bergman T., Lavine A., Incropera F., DeWitt F., “Introduction to Heat Transfer”, 6th Edition, 2011.

Escobar S., 2014,”Development of a liquid test bench for cold plate characterization”, HP internal reports.

Ferrer E., 2016, “Vapor chamber CFD studies”, PI-HPE internal report.

Holman J.P., “Experimental Methods for Engineers”, 6th Edition, 1994.

Muzychka Y.S., Culham J.R., Yovanovich M.M., 2003, “Thermal spreading resistance of eccentric heat sources on rectangular flux channels”, Journal of heat transfer Transactions of the ASME, Vol. 125, pp. 178-185

Prasher R., 2003, “Simplified conduction based modeling scheme for design sensitivity study of thermal solution utilizing heat pipe and vapor chamber technology”, Journal of electronic packaging, Transactions of the ASME, Vol. 125, No. 3

Rao Tummala, Eugene J. Rymaszewski, Alan G, 1997, Microelectronics Packaging Handbook: Technology Drivers, Part 1.

Wei X., Sikka K., 2006, “Modeling of vapor chambers as heat spreading devices”, 10th Intersociety conference on thermal and thermomechanical phenomenain electronics systems.